Electrochimica Acta 269 (2018) 144–154

Contents lists available at ScienceDirect

Electrochimica Acta

journal homepage: www.elsevier.com/locate/electacta

Facilitating high-capacity V_2O_5 cathodes with stable two and three Li^+ insertion using a hybrid membrane structure consisting of amorphous V_2O_5 shells coaxially deposited on electrospun carbon nanofibers

Emery Brown [a], Seok-Hwan Park [a, b], Ayyappan Elangovan [a], Yue Yuan [c], Jooyoun Kim [c, d], Xiuzhi Susan Sun [e], Xiaoming Zhang [f], Guohong Wang [f], Jun Li [a, f, *]

[a] Department of Chemistry, Kansas State University, Manhattan, KS 66506, USA
[b] Department of Chemical Engineering, Pohang University of Science and Technology, Pohang, 37673, South Korea
[c] Department of Apparel, Textiles, and Interior Design, Kansas State University, Manhattan, KS 66506, USA
[d] Department of Textiles, Merchandising and Fashion Design, College of Human Ecology, Seoul National University, Gwanak-gu, Seoul 08826, South Korea
[e] Department of Grain Sciences and Engineering, Kansas State University, Manhattan, KS 66506, USA
[f] College of Chemistry and Chemical Engineering, Hubei Normal University, Huangshi, Hubei 435002, PR China

ARTICLE INFO

Article history:
Received 8 December 2017
Received in revised form
8 February 2018
Accepted 27 February 2018
Available online 2 March 2018

Keywords:
Lithium ion battery
Vanadium pentoxide
Carbon nanofiber network
Electrospinning
Pulsed electrodeposition

ABSTRACT

This study reports an approach to achieving stable 2 and 3 Li^+ insertion, respectively, into vanadium pentoxide (V_2O_5) as lithium-ion battery (LIB) cathode materials using a core-shell structure based on a self-standing carbon nanofiber (CNF) membrane fabricated by an electrospinning process. Uniform coaxial V_2O_5 shells are coated onto continuous CNF cores via a pulsed electrodeposition. The materials analyses confirm that the V_2O_5 shell after 4 h of thermal annealing at 300 °C forms a partially hydrated amorphous structure. SEM and TEM images indicate that the uniform 30–50 nm thick V_2O_5 shell forms an intimate interface with the CNF core. Lithium insertion capacities up to 291 and 429 mAh g^{-1} are achieved in the voltage ranges of 4.0–2.0 V and 4.0–1.5 V, respectively, which are in good agreement with the theoretical values of 294 mAh g^{-1} for 2 Li^+/V_2O_5 insertion and 441 mAh g^{-1} for 3 Li^+/V_2O_5 insertion into crystalline V_2O_5 materials. Moreover, after 100 cycles, remarkable retention rates of 97% and 70% are obtained for 2 Li^+/V_2O_5 and 3 Li^+/V_2O_5 insertion, respectively. These results reveal that it is potentially feasible to fabricate the core-shell structure with electrospinning and electrodeposition processes to break the intrinsic limits of V_2O_5 and enabling this high-capacity cathode materials for future LIBs.

1. Introduction

Electrical energy storage (EES) technologies play a major role in todays' society owing to the advances in hybrid and electric cars [1], the ever-growing demand for portable electronic devices [2], and grid-leveling for energy generated by intermittent renewable sources [3]. Lithium ion batteries (LIBs) have dominated the EES market for the past several decades [4,5]. However, there are growing demands to improve LIBs for higher energy and power densities. These critically depend on electrode materials and architectures. Particularly, the low specific capacity of cathode materials is currently the bottleneck limiting the energy storage capability of LIBs [6]. Most commercial LIBs can achieve a near theoretical specific capacity of 372 mAh g^{-1} with a graphite anode and even higher values with emerging anode materials such as Si [7–9], while only ~140–170 mAh g^{-1} can be achieved with the cathode (such as $LiCoO_2$, $LiFePO_4$, etc) [6]. Hence, developing novel cathode materials with higher charge storage capacity is one of the top priorities in LIB research [10,11].

Vanadium pentoxide (V_2O_5) had been studied as a candidate for a high-capacity cathode material owing to its low cost, low toxicity, high delithiated electrode potential (up to 4.0 V), and easily accessible layered structure for Li^+ ion insertion [12]. Crystalline V_2O_5 can achieve a reversible specific capacity of 294 mAh g^{-1} for a two Li^+/V_2O_5 insertion process. However, three Li^+/V_2O_5 insertion was found to be highly irreversible even though a high insertion

* Corresponding author. Department of Chemistry, Kansas State University, Manhattan, KS 66506, USA.
E-mail address: junli@ksu.edu (J. Li).

https://doi.org/10.1016/j.electacta.2018.02.167
0013-4686/

capacity of 441 mAh g^{-1} was observed in the first cycle [13–15]. It is well known that the Li^+ intercalation process in crystalline V_2O_5 is accompanied by multiple phase transitions [13,14]. Trace amounts of Li^+ intercalation results in α-$Li_xV_2O_5$ ($x < 0.01$) structure, which is transformed into ε-$Li_xV_2O_5$ ($0.35 < x < 0.7$) after further lithiation. Insertion of one Li^+ leads to the formation of δ-phase $Li_xV_2O_5$ ($x = 1$). Further lithiation converts the δ-phase to γ-$Li_xV_2O_5$ ($1 < x < 2$). At more than two Li^+ insertions, an irreversible transformation to rock-salt-type ω-$Li_xV_2O_5$ phase ($2 < x < 3$) occurs [13,14]. Even below 2 Li^+/V_2O_5 insertion, such phase transition processes induce large strains in the particles, causing irreversible structural damage and quick capacity fading [13,14]. Insertion up to 3 Li^+/V_2O_5 makes such structural changes even more severe. As a result, practical applications of crystalline V_2O_5 cathodes have been hindered [13,14]. In recent years, V_2O_5 gained renewed interests due to the evidence that the lattice strains and structural collapse can be largely circumvented with nanostructured morphology [14,16,17]. Particularly, the traditionally neglected amorphous V_2O_5 has shown potential for better stability and higher Li^+ insertion capacity than crystalline V_2O_5, even possible to exceed 3 Li^+/V_2O_5 insertion [18,19].

Besides the complicated phase transitions, lithium insertion/extraction in V_2O_5 cathodes has also been limited by the intrinsic properties of V_2O_5. Crystalline V_2O_5 materials have small Li^+ ion diffusion coefficients (~$10^{-15} - 10^{-12}$ cm^2 s^{-1}) and low electrical conductivities (~$10^{-5} - 10^{-3}$ S cm^{-1}) [20,21]. Amorphous V_2O_5 may provide a higher Li^+ diffusion coefficient, but at the price of sacrificing the electrical conductivity and mechanical strength. Two strategies have so far been employed to overcome the intrinsic limits of V_2O_5, mostly with crystalline materials. The first one is to mitigate the low Li^+ ion diffusion coefficients by using low-dimensional nanostructures [14,20,22–26]. This strategy increases the overall specific surface area (SSA) and provides shorter diffusion pathways for Li^+ ions. In addition, low-dimensional nanostructures can also partially relieve the large lattice strain during the phase transitions and significantly extend the battery life. However, the electrical contact between V_2O_5 nanoparticles may degrade and become a dominant factor. The second strategy (often combined with the first one) is to incorporate low dimensional conductive carbon materials such as multiwall carbon nanotubes (MWCNTs) [27–31], graphene [20,32], and reduced graphene oxide (rGO) [33–38] to form nanocomposite materials. The addition of these conductive additives prevents aggregation and enhances the effective electrical conductivity throughout the electrode material. However, the poor electrical contact at the interface of the V_2O_5 nanoparticles and carbon additives and the lack of a continuous carbon framework still limit these materials from reaching high capacity at higher power rates.

Recently continuous core-shell structures have been investigated by depositing V_2O_5 thin shells using atomic layer deposition (ALD) [39] or ion sputtering [40] onto preformed three-dimensional (3D) nanostructured carbon templates. In such binder-less 3D core-shell structures, the highly conductive carbon framework has been retained as a continuous electrical pathway to effectively collect electrons from the active materials in the thin shells. The robust carbon core also improves the mechanical stability of the electrode. Here we extend this concept into a potentially scalable process based on electrodeposition of V_2O_5 shells onto a self-supported carbon nanofiber (CNF) membrane fabricated by electrospinning. The pulsed electrodeposition process enables formation of a uniform coaxial V_2O_5 shell of 30–50 nm in thickness on the CNF surface throughout the entire mesoporous membrane. With proper thermal treatment, the V_2O_5 shell was converted into a partially hydrated amorphous structure. The core-shell structure was found to be effective in overcoming the poor mechanical stability and low electrical conductivity of the disordered V_2O_5 shell. The lithium storage capability of such core-shell materials was found to be superior to traditional crystalline V_2O_5 materials. The half-cell characterization in the potential range of 4.0–2.0 V (vs. Li/Li^+) showed a capacity up to 291 mAh g^{-1}, matching the theoretical value for 2 Li^+/V_2O_5 insertion/extraction with a remarkable capacity retention rate of 97% after 100 cycles. When extending the lower potential limit to 1.5 V (vs. Li/Li^+), reversible 3 Li^+/V_2O_5 insertion/extraction up to 429 mAh g^{-1} was achieved, with 70% of the capacity retained after 100 cycles. These results demonstrate that the core-shell structure may enable the traditionally unfavored amorphous V_2O_5 material to surpass crystalline V_2O_5 for future high-capacity LIB cathodes.

2. Experimental

2.1. CNF formation and pulsed electrodeposition of V_2O_5

CNFs were prepared using a simple electrospinning method followed by post thermal annealing as reported before [41,42]. Briefly, 0.8 g of polyacrylonitrile (PAN) was dissolved in 8.0 g of N, N-dimethylformamide (DMF) at 120 °C under vigorous stirring for 1 h. The resulting solution was cooled to room temperature and loaded into a syringe and electrospun into polymer fibers on a Spraybase® system (Profector Life Sciences, Cambridge, MA). After continuous electrospinning for 5 h at a flow rate of 1 mL/h and an applied electric field strength of 1 kV/cm (with 18 kV voltage bias at a nuzzle-collector distance of 18 cm), a letter paper sized membrane is collected on an aluminum foil wrapped on the rotating drum. The resulting polymer membrane was stabilized in air at 280 °C for 2 h followed by carbonization at 1000 °C for 1 h under nitrogen, forming a continuous CNF membrane. The CNF membrane was then used as a working electrode during pulsed electrodeposition in a three-electrode electrochemical cell, where a Pt foil and a Ag/AgCl (4 M KCl) were used as the counter and reference electrodes, respectively, under control by a Parstat 2273 Analyzer (Princeton Applied Research Corporation, Oak Ridge, TN). The composition of the V_2O_5 sol electrolyte was modified from a previous report [43], with 0.91 g of V_2O_5 powder dissolved in 50 mL of deionized (DI) water and 4.5 mL of 30% hydrogen peroxide by vigorous stirring at room temperature for 1 h. To achieve uniform V_2O_5 shells across the entire 60 μm thick CNF membrane, a novel pulsed electrodeposition was implemented. The electrode potential was first set at 0 V for 20 s to establish electrolyte equilibrium and then followed by −2.0 V for 10 s for electrophoretic deposition of V_2O_5. This sequence was repeated for 60 cycles. The resulting CNF–V_2O_5 core-shell membrane was dried in air for 1 h at 70 °C followed by thermal annealing at 300 °C for 4 h in air. Several samples were further annealed for an additional 20 h in air at 300 °C to burn out the carbon and leave only the hollow crystalline V_2O_5 shell for the purpose of materials characterization.

2.2. Materials characterization

The surface morphology of the bare CNFs and the thin V_2O_5 shells was examined with a Helios NanoLab 660 (FEI, Hillsborro, OR) field emission scanning electron microscope (FESEM) which was equipped with a focused ion beam apparatus to create cross sections of the sample. High resolution transmission electron microscopy (HRTEM) and scanning transmission electron microscopy (STEM) with high-angle annular dark-field (HAADF) images were obtained using a FEI Tecnai Osiris (S)TEM system (FEI, Hillsborro OR) to further evaluate the crystal structure of the outer V_2O_5 shell. Elemental analysis and mapping were carried out using energy-dispersive X-ray spectroscopy (EDS) in the TEM to show

uniformity of the V_2O_5 shell along the CNF. Raman spectra were obtained using a Renishaw inVia confocal Raman microscope (Gloucestershire, UK) with a laser wavelength of 532 nm. The crystallinity was evaluated using a Rigaku SmartLab (The Woodlands, TX) X-ray diffractometer. Diffraction analysis was conducted from 10° to 60° using a Cu Kα source with a wavelength of 1.541 Å. Brunauer–Emmett–Teller (BET) measurements were carried out with a ASAP 2460 Surface Area and Porosity Analyzer (Norcross, GA) to determine the specific surface area (SSA) and porosity. Thermal gravimetric analyses (TGA) were carried out using a TA Instrument Q50 (New Castle, DE) from room temperature to 800 °C in air at a rate of 5 °C/min.

2.3. Electrochemical characterization

To evaluate the electrochemical performance of the CNF–V_2O_5 cathode, half-cells were assembled into stainless steel coin cells (CR2016, MTI Corporation, Richmond, CA). The CNF–V_2O_5 core-shell porous membrane was used as a self-supported binder-less cathode against a 16-mm dia. lithium disk anode electrode which were separated by a 0.65 mm thick glass fiber separator (El-Cell, Hamburg, Germany). The cell was assembled in an argon filled M-Braun LabStar50 stainless steel glovebox (Garching, Germany) with water and oxygen contents less than 0.5 ppm. The CNF–V_2O_5 core-shell membrane (2.4 mg) was adhered to an aluminum current collector using a thin layer of inert "glue" made of ~0.1 mg Super P and ~0.1 mg polyacrylic acid (PAA) in ~0.5 mL solution of N-Methyl-2-pyrrolidone (NMP). The mass of the applied "glue" was only 2–5% of the CNF–V_2O_5 core-shell membrane and serve only for the purpose to retain the membrane in place during cell assembly. The adhered CNF–V_2O_5 core-shell membrane was then dried for 1 h at 70 °C under vacuum prior to cell assembly. The contribution of the inert glue to the overall capacity is negligible. The electrolyte consisted of 1.0 M lithium hexaflourophosphate ($LiPF_6$) in a mixture of 1:1:1 vol ratio ethylene carbonate (EC), ethyl methyl carbonate (EMC), and dimethyl carbonate (DMC) with a 2% vinylene carbonate additive (Novolyte, Ohio). Galvanostatic charge-discharge cycles were performed using a MTI 8 channel battery analyzer (MTI Corporation, Richmond CA). All gravimetric capacities were calculated relative to the mass of V_2O_5 that was determined by TGA. Cyclic voltammetry (CV) and electrochemical impedance spectroscopy (EIS) measurements were performed using a CHI760D potentiostat (CH Instruments, Austin, TX).

3. Results and discussion

3.1. SEM/TEM characterization of the CNF–V_2O_5 core-shell structure

A low-magnification SEM image of the bare CNF membrane is shown in Fig. 1a. Clearly, CNFs form an entangled network with random stacking and large inter-CNF pores (varying from ~1 to 3 μm). Two high-magnification SEM images of the side and cross-sectional views of bare CNFs are shown in Figs. S1a and S1b, respectively. From these images, the majority of the bare CNFs have the diameter spreading between ~100 nm and ~400 nm with the average value at ~250 nm. The thickness of the CNF membrane was estimated to be 50–60 μm as shown in the SEM images in Fig. S1c and d. A high-magnification SEM image of the cross-section of a single CNF deposited with a V_2O_5 shell is shown in Fig. 1b. It is clear that the V_2O_5 (illustrated by the white arrow) forms an intimate interface with the CNF core, showing no visible boundaries at the cross section. A SEM image at a low accelerating voltage (3 kV) in Fig. 1c shows that the V_2O_5 shell is a continuous porous layer with slightly larger outer surface roughness than the original CNF cores. Additional SEM images in Fig. S2 further illustrate the uniform coaxial deposition of V_2O_5 shells throughout the CNF membrane. Furthermore, the SEM image at a higher accelerating voltage (10 kV) in Fig. 1d shows better contrast between the outer V_2O_5 layer and the CNF cores. Particularly, the area inside the red circle where fiber 1 crosses atop fiber 2 clearly shows about 30–50 nm thin conformal V_2O_5 coating on the CNF cores.

To further evaluate the V_2O_5 shell, the sample was annealed at 300 °C in air for a prolonged time of 24 h. SEM images in Fig. 1e and f confirm that the CNF cores were burnt out, leaving only the crystalized V_2O_5 shells as hollow tubes. The polycrystalline V_2O_5 tube is apparently rougher than the 4-h annealed sample in which V_2O_5 shells retain the as-deposited morphology. The digital photographs show that the membrane changes from a black color similar to that of the bare CNFs (Fig. 1g) to the bright yellow color reminiscent of orthorhombic crystalline V_2O_5 (Fig. 1h).

A HRTEM image of the 4-h annealed CNF–V_2O_5 core-shell structure is shown in Fig. 2a. The outer V_2O_5 layer is visible along the CNF core as highlighted by the white brackets. Additional HRTEM images are shown in Fig. S3 with white dash lines added in Fig. S3b as visual guides to differentiate the inner CNF core and the outer V_2O_5 shell. A TEM image of the hollow V_2O_5 shell after carbon burnout is shown in Fig. 2b. A high-angle annular dark-field (HAADF) STEM image of the 4-h annealed CNF–V_2O_5 core-shell structure is shown in Fig. 2c. The lack of sharp diffraction spots in the selective area electron diffraction (SAED) pattern in the inset of Fig. 2c confirms that both CNF and V_2O_5 are amorphous or highly disordered. In contrast, the SAED of the hollow V_2O_5 shell after prolonged annealing in inset of Fig. 2d shows sharp diffraction spots, which indicates the formation of a crystalline V_2O_5 structure. Due to the large V_2O_5 tube diameter and shell thickness, the HRTEM image (Fig. 2d) only shows the texture of the crystalline V_2O_5 but not the atomic lattices. The EDS spectrum in Fig. S4 shows that the CNF–V_2O_5 core-shell material is dominated by C, O, N, and V elements. The N atoms are likely residue from the starting PAN precursors in electrospinning. Elemental mapping in Fig. 2e–g and the line profiles in Fig. S5 confirm the uniform distribution of C, O and V elements in the core-shell nanofibers.

It is noteworthy that the observed uniform coaxial V_2O_5 coating on each CNFs throughout the membrane is highly desired for effective current collection. Due to the high density and heavy entanglement of the CNF membrane (as shown in Fig. S1c and d), V_2O_5 deposition is limited by mass transport. Materials opt to deposit much faster at the outer surface of the membrane in normal continuous electrodeposition at a constant potential or current, leading to capping the outer surface and insufficient deposition inside the CNF membrane. Such uneven deposition was avoided in this study by adopting a unique pulse electrodeposition method similar to our previous studies [44,45]. Fig. S6a and b show the experimental setup and a CV curve of the CNF membrane in the V_2O_5 sol solution. During electrodeposition, the electrode potential was first set at −2.0 V for 10 s (the "on" time) to deposit a sub-nanometer thick V_2O_5 layer throughout the CNF network. A longer "off" time of 20 s then followed, with the electrode potential at 0 V, which stopped V_2O_5 deposition and allowed fresh electrolyte to diffuse into the membrane and re-establish the concentration equilibrium. These two steps alternatively repeated 60 times to obtain the desired V_2O_5 quantity. The current profiles in Fig. S6c and d indicate that the pulsed electrodeposition process is highly reproducible except the first few cycles. The quantity of V_2O_5 deposition can be controlled by varying the number of cycles. The schematic diagram in Fig. S7 illustrates the effects on the deposition uniformity across the CNF membrane by the common constant voltage vs. the pulsed electrodeposition.

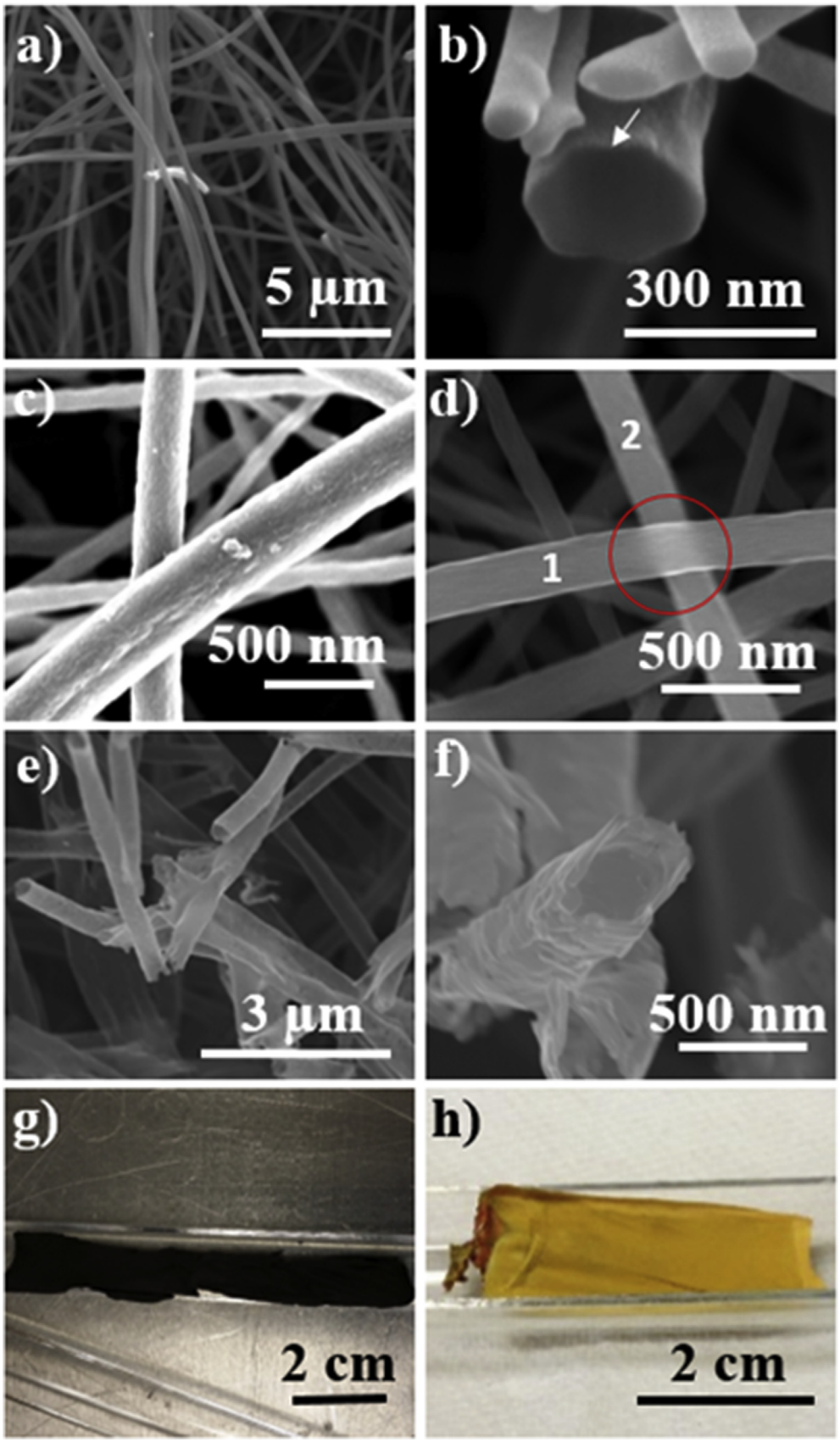

Fig. 1. Low-magnification SEM images of a) a bare CNF membrane and b) the cross-section of a single CNF–V_2O_5 core-shell nanofiber. SEM images at accelerating voltages of c) 3 kV and d) 10 kV showing the thin coating of V_2O_5 at the surface of CNFs. e) Low- and f) high-magnification SEM images of hollow V_2O_5 shells after burning out CNF cores by the prolonged thermal annealing. Digital photograph images of g) a bare CNF membrane and h) a hollow V_2O_5 shell membrane.

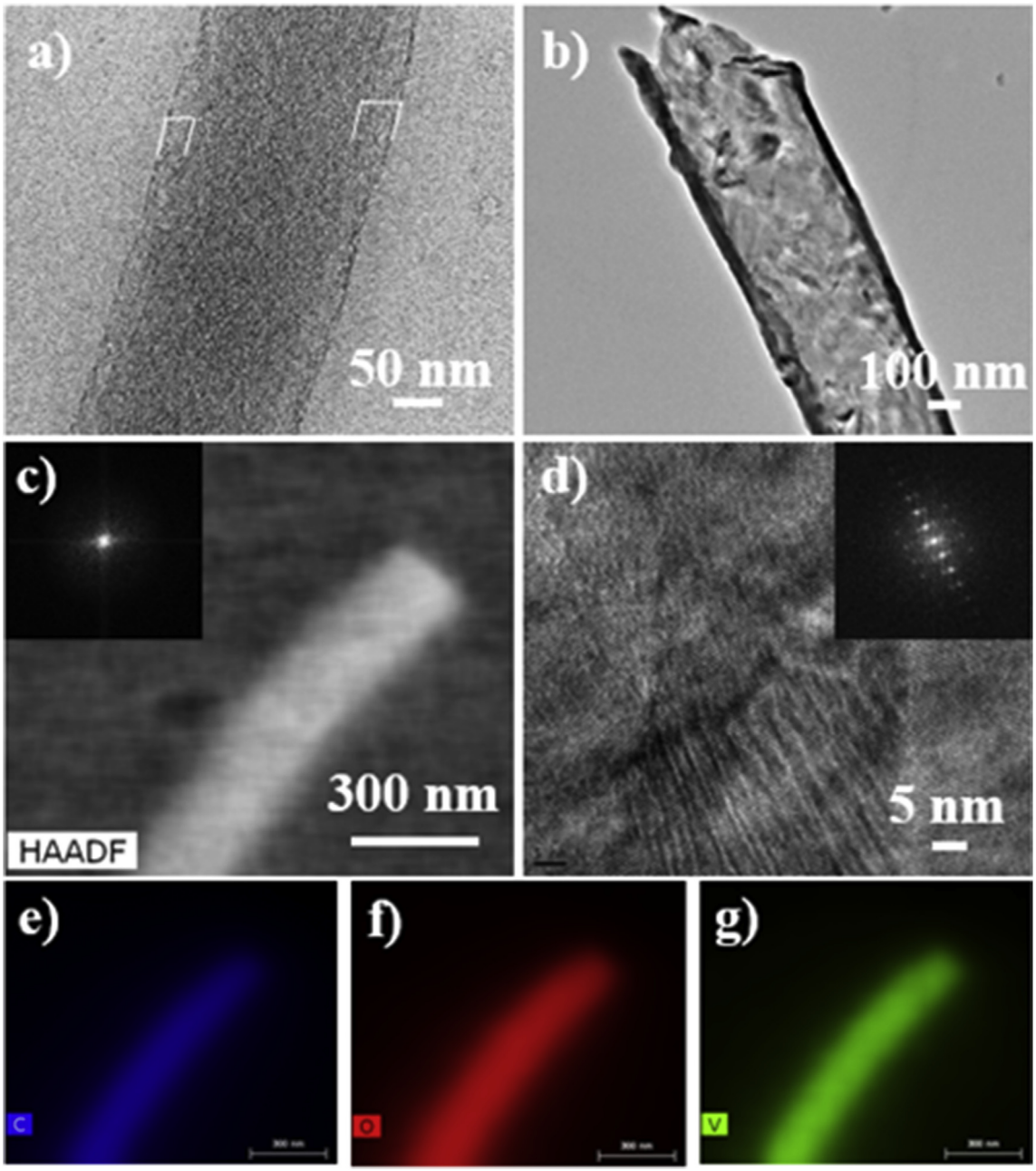

Fig. 2. TEM images of a) a CNF–V_2O_5 core-shell structure and b) a hollow V_2O_5 shell after burning out the CNF core. c) A HAADF STEM image of a CNF–V_2O_5 core-shell structure. d) A HRTEM image of a hollow V_2O_5 shell. EDS mapping of the single CNF–V_2O_5 nanofiber in panel (c) showing the presence of e) carbon, f) oxygen, and g) vanadium. The scale bars in panel (e) to (g) are 300 nm. The insets in panels (c) and (d) are selected area electron diffraction patterns.

3.2. Materials characterization of the CNF–V_2O_5 core-shell structure

The Raman spectra of the CNF–V_2O_5 core-shell structure in Fig. 3a shows the characteristic peaks of V_2O_5 (at 140, 282, 403, 513, 696, and 993 cm^{-1}) which match well with pure α-V_2O_5 nanopowders [46]. The peak at 990 cm^{-1} corresponds to the stretching mode of the vanadyl V═O double bond, which does not exist in the lower oxidation states of vanadium oxides. The stretching mode of V–O–V corresponds to the peak at 696 cm^{-1}. The peaks located at 513 and 403 cm^{-1} are assigned to the bending vibration of V_2–O and the V═O bonds of α-V_2O_5, respectively. The well-defined peak at 282 cm^{-1} corresponds to the bending vibration of V═O bonds of α-V_2O_5. The peak at 143 cm^{-1} corresponds to the long range external mode α-V_2O_5, suggesting pockets of long range order in the mostly disordered structure. These results suggest that the 4-h annealed samples are dominated by the chemical bonds of V_2O_5 [47,48], even though the crystal structure was highly disordered (or amorphous). The peaks at 1351 and 1614 cm^{-1} correspond to the D and G bands of the CNF core. Clearly, both disordered sp^3 and graphitic sp^2 carbon present in the CNFs.

The XRD analysis of the 4-h annealed CNF–V_2O_5 core-shell structure (blue) and 24-h annealed hollow V_2O_5 shells (red) in Fig. 3b show the dramatic effects of annealing time on the crystal structure. The CNF–V_2O_5 core-shell structure shows a very broad asymmetric peak which can be de-convoluted into a small peak at

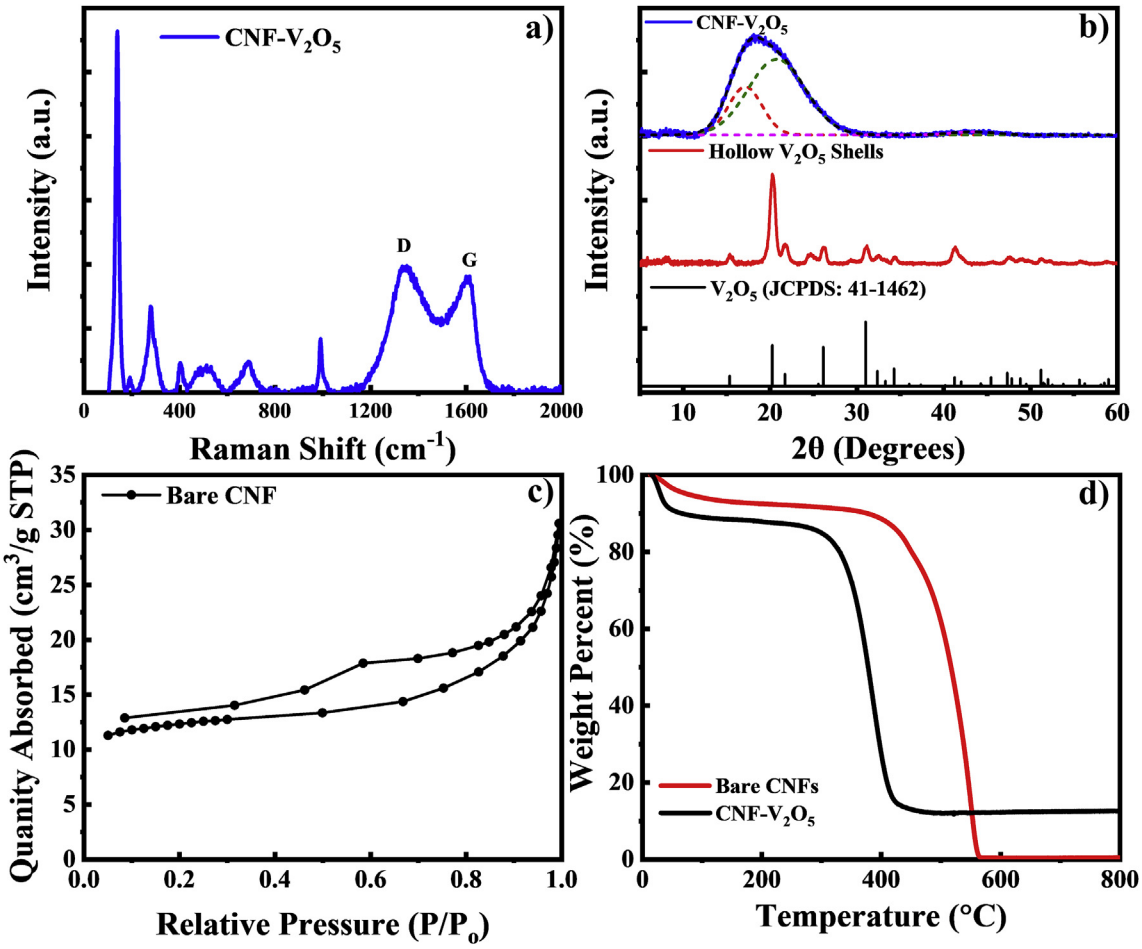

Fig. 3. a) Raman spectrum of the CNF–V2O5 core-shell structure. b) XRD patterns of the CNF–V_2O_5 core-shell structure (blue) and hollow V_2O_5 shells (red). c) BET measurements of bare CNFs. d) TGA measurements of bare CNFs and the CNF–V_2O_5 core-shell material. (For interpretation of the references to color in this figure legend, the reader is referred to the Web version of this article.)

17.15° and a large peak at 20.77°, respectively. The d-spacing values are 5.17 and 4.27 Å, respectively, corresponding to the interlayer distance of the V_2O_5 shell and the disordered graphitic carbon core. The d-spacing of 5.17 Å is larger than the 4.37 Å inter-layer spacing of orthorhombic α-V_2O_5 crystals, which is likely due to the presence of a certain degree of hydration in V_2O_5 [49]. The coherent length calculated from the de-convoluted XRD peak width is 1.96 nm (about a stack of only 5 V_2O_5 atomic layers), consistent with amorphous properties observed with SAED of TEM. It's worth noting that the d-spacing of CNF (4.27 Å) is significantly larger than that of graphite (3.43 Å), and in conjunction with a coherent length of only 1.16 nm (about a stack of ~4 carbon layers). The high degree of disorder is consistent with the Raman spectroscopy. A zoom-in plot of the deconvoluted XRD peak of the CNF–V_2O_5 core-shell structure is presented in Fig. S8. The weak peak at 2θ of 43.3° can be attributed to the (002) peak of graphitic layers. In contrast, the hollow V_2O_5 shells after prolonged annealing show sharp diffraction peaks that can be attributed to the highly crystalline orthorhombic phase of α-V_2O_5, which is consistent with the pattern of JCPDS: 41–1426 database. It should be noted that a weak peak at 24.74° was observed after the prolong annealing, which is attributed to residual graphitized carbon with a smaller d-spacing of 3.60 Å.

The N_2 adsorption/desorption isotherm for the bare CNFs is shown in Fig. 3c, indicating a mesoporous structure. The BET surface area was determined to be 38.5 $m^2 g^{-1}$. After V_2O_5 deposition, the BET isotherm showed similar features with an increased surface area of 42 $m^2 g^{-1}$, but the pore radius distribution shifted from the range of 2–8 nm to 6–12 nm (see Fig. S9). The small increase in surface area after V_2O_5 deposition is attributed to the porosity of the disordered V_2O_5 and outer surface roughness. The composition and thermal stability of the samples were investigated with TGA shown in Fig. 3d, at a rate of 5 °C/min. For both bare CNFs and the CNF–V_2O_5 core-shell structure, a loss of 5% and 10%, respectively, was observed below 100 °C, due to desorption of physisorbed gas molecules (mostly water due to the high humidity in the environment). Such water sorption in the porous materials is unavoidable since the samples were stored and transported in the air prior to TG measurements. Bare CNFs started burning out at ~400 °C and were completely gone at ~560 °C. In contrast, the CNF–V_2O_5 core-shell structure started to lose the carbon materials near ~300 °C and the mass rapidly dropped to ~12% at ~450 °C and remained stable at this value up to ~800 °C. As indicated by the SEM and TEM images in Figs. 1 and 2, the main CNF core was retained for thermal annealing at ~300 °C for 4 h while the quality of both CNF core and V_2O_5 shell is improved. The mass above 450 °C can be attributed entirely to crystalline V_2O_5. The shift in the initial carbon burning temperature can be attributed to the proximity of the oxygen source from metal oxides which are in direct contact with carbon as well as possible catalysis by vanadium, which deserve further study in the future. The V_2O_5 percentage varied from ~10% to 30% in samples prepared in different days which were mainly

due to slow drift of the reference electrode potential (by about 20–40 mV). Thus, all specific capacities in later LIB tests were calculated using the actual V_2O_5 mass determined by the TGA analyses of each sample.

3.3. Assessment of 2 Li^+/V_2O_5 insertion/extraction between 4.0 and 2.0 V (vs. Li/Li^+)

The Li-ion storage properties of the above described CNF–V_2O_5 core-shell structure was systematically characterized in the half-cell configuration using CR2016 coin cells. An 18-mm diameter disk was punched out from the CNF–V_2O_5 membrane and glued onto an Al disk of the same diameter and used as the cathode (see Fig. S10). The as-assembled cell is in the charged state with a cell voltage in the range of 2.3–3.3 V. A galvanostatic discharge process was carried out first and followed by alternating charge/discharge measurements at different current rates at fixed potential windows. Columbic efficiency was calculated as the percentage ratio of the discharge (Li^+ insertion) capacity to the charge (Li^+ extraction) capacity in the prior step. Typically, C rates (rather than current densities) are used in literature for battery characterization. To avoid confusion, in this paper, all referred C rates are based on the actual time to complete a full charge or discharge process at the specific current density, with a rate of C/n corresponding to the condition to complete a charge or discharge in n hours. For $n \leq 1$, an alternative notation (1/n)C is used for simplicity. To better assess the materials properties and compare them with the theoretical values, only the mass of V_2O_5 is used for calculating the gravimetric capacity in this study. The contribution of the CNF network to Li storage is negligible in the studied potential range.

The CNF–V_2O_5 core-shell structure was first investigated for 2 Li^+ insertion per V_2O_5 formula with galvanostatic charge-discharge measurements in the voltage range of 4.0–2.0 V (vs. Li/Li^+) as shown in Fig. 4a. Cells were discharge/charged for 25 cycles each at 5 different current densities (100, 250, 500, 750, and 1000 mA g^{-1}) before returning to the initial current rate (100 mA g^{-1}) at cycle 26. The first five cycles at 100 mA g^{-1} (~C/3 rate) were unstable with an insertion capacity of 291 mAh g^{-1} and a coulombic efficiency of 94% at cycle 5. The insertion (discharge) capacity at this low rate matches well with the theoretical capacity of 294 mAh g^{-1} for 2 Li^+/V_2O_5 insertion process [14]. When the rate was increased to 250 mA g^{-1} (~1C rate), the cell was stabilized with an insertion capacity of 242 mAh g^{-1} and a higher coulombic efficiency to 97%. High insertion capacities of 217, 207, and 198 mAh g^{-1} were obtained at rates of 500 (2.3C), 750 (3.6C), and a 1000 (5.1C) mA g^{-1}, respectively. Interestingly, as the rate was increased to 1000 mA g^{-1}, the coulombic efficiency increased to ~99%. Generally, the coulombic efficiency decreases at higher current rates in literature. Here the coulombic efficiency increases with increasing current rates which can be attributed to the better current collecting capability and faster reaction kinetics with the core-shell structure. It is also likely that a high pseudocapacitance contribution aids in the high coulombic efficiency at the high rates. When the current was reduced back to 100 mA g^{-1} in cycles 26–30, a stable insertion capacity of 290 mAh g^{-1} was achieved, resulting in a capacity retention of ~99% comparing to cycle #5. Insertion capacities of 240, 215, 203, and 194 mAh g^{-1} were obtained at current rates of 250, 500, 750, and 1000 mA g^{-1}, respectively, in cycles 31–50. These values are all comparable to those in cycles 6–25 of the first set of rate-performance tests, demonstrating the high stability of the CNF–V_2O_5 core-shell structure. It is notable that the capacity only dropped by ~32% as the charge-discharge current was increased 10 times from 100 to 1000 mA g^{-1}.

A representative Nyquist plot of electrochemical impedance spectroscopy (EIS) measurements at the charged state (~4.0 V) was obtained after 5 cyclic voltammetry cycles (1 mV/s) as shown in Fig. S11. An equivalent series resistance of 53.33 Ohm (R_1) and a charge transfer resistance of 170.8 Ohm (R_3) was derived from the fitted circuit, which are a little bit high and expected for amorphous V_2O_5 materials. The capacitance value of the constant phase element (CPE, represented by Q_2) corresponding to the CNF–V_2O_5 electrode was derived to be only 4.6 μF, indicating a low EDLC contribution from the CNF framework. The R_3 value of 80.18 Ohm and the capacitance value 8.8 μF in the first CPE (Q1) likely originated from the Li counter electrode. The cell performance likely can be further improved in the future by optimizing the electrical contact in the core-shell nanofiber membrane.

The galvanostatic charge-discharge curves of the last cycle at current rates of 100 (black), 250 (red), 500 (blue), 750 (magenta), and 1000 (green) mA g^{-1} in the rate-performance tests are presented in Fig. 4b. All profiles show nearly linear curves without clear flat plateaus that are commonly seen for Li^+ insertion/extraction in crystalline V_2O_5, indicating that the system behaved like a pseudocapacitor. These properties explain the high stability and high coulombic efficiency at the high applied current rates. The high degree of pseudocapacitance contribution is also seen in the CV curves in Fig. 4c. Only a small reduction peak was observed between 3.2 and 3.0 V corresponding to the crystalline phase transformation from α-V_2O_5 to ε-$Li_xV_2O_5$ ($0.35 < x < 0.7$) and δ-LiV_2O_5. The two reduction peaks commonly observed in crystalline V_2O_5 [14] were superimposed in this study owing to the amorphous nature of V_2O_5. A larger reduction peak was observed at 2.3 V at a scan rate of 0.1 mV s^{-1} corresponding to the phase transformation from δ-LiV_2O_5 to γ-$Li_2V_2O_5$. During the extraction process, only a single oxidation peak was observed at 3.0 V corresponding to the phase transformation of γ-$Li_2V_2O_5$ back to δ-LiV_2O_5. Two small oxidation peaks followed at ~3.4 and 3.6 V corresponding to the phase transformation from δ-LiV_2O_5 to ε-$Li_xV_2O_5$ ($0.35 < x < 0.7$) and α-V_2O_5, respectively. Compared with the CVs of crystalline V_2O_5 materials, the CNF–V_2O_5 core-shell structure present a large baseline separation between the charge and discharge currents, reflecting the dominant pseudocapacitive properties associated with the amorphous V_2O_5 shells. Fig. 4d further demonstrates the remarkable stability of the CNF–V_2O_5 core-shell structure in 100 charge/discharge cycles at 100 mA g^{-1} (~C/3 rate). A stable capacity of 292 mAh g^{-1} was obtained at cycle 10 which only slightly decreased to 282 mAh g^{-1} in cycle 100, resulting in a high capacity retention of 97%.

It is noteworthy that current LIBs are mainly focused on ordered crystalline materials due to ordered Li^+ ion pathways and well-defined redox reactions. Even though enhanced capacity was obtained with disordered oxide materials [50] (including hydrated V_2O_5 [16,51,52]), these materials are limited by the poor mechanical stability, low electrical conductivity and tortuous ion pathways. Using core-shell hybrid structures in which thin V_2O_5 shells coated on stable nanostructured carbon cores has been demonstrated as an effective approach to overcoming these issues [39]. Particularly, we have previously demonstrated that partially hydrated amorphous V_2O_5 shells deposited on vertically aligned carbon nanofiber (VACNF) arrays provided over 30% higher capacity than crystalline V_2O_5 shells in highly stable 2 Li^+/V_2O_5 processes [40]. The results of the electrospun CNF–V_2O_5 core-shell structure in this study further validate the effectiveness of the core-shell hybrid approach. Furthermore, electrospinning is a potentially scalable technique which can be adapted for future LIB production.

3.4. Assessment of 3 Li^+/V_2O_5 insertion/extraction between 4.0 and 1.5 V (vs. Li/Li^+)

To explore the potential for even higher capacity, we further

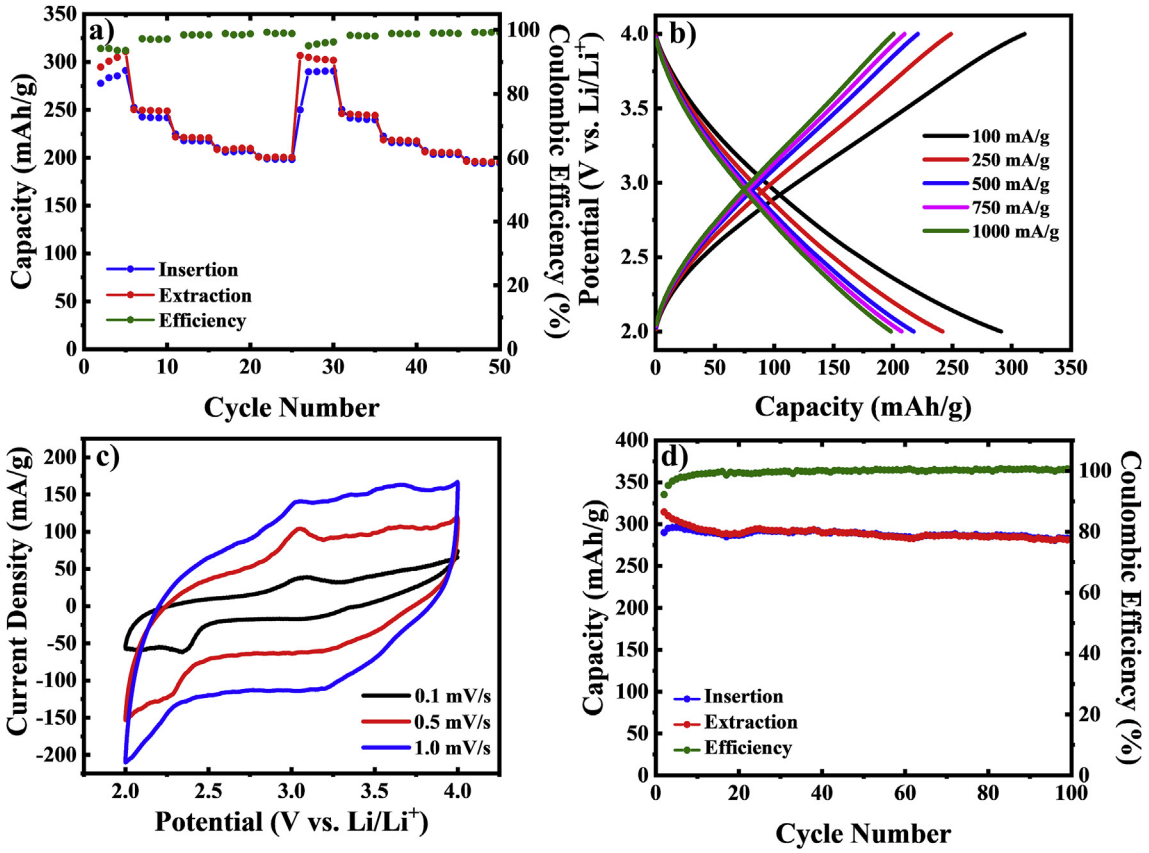

Fig. 4. Electrochemical characterization of the 2 Li^+/V_2O_5 insertion/extraction. a) Rate performance of the CNF–V_2O_5 core-shell structure in the potential range of 4.0–2.0 V (vs. Li/Li^+) at 5 different current density values (100, 250, 500, 750, and 1000 mA g^{-1}), each with 5 charge-discharge cycles. b) The galvanostatic charge-discharge profiles of the last cycle at each current density in the rate-performance tests. c) Cyclic voltammetry curves at 0.1 (black), 0.5 (red) and 1.0 (blue) mV s-1 in the potential range of 4.0–2.0 V (vs. Li/Li^+). d) Long-term cycling at a rate of 100 mA g^{-1}. (For interpretation of the references to color in this figure legend, the reader is referred to the Web version of this article.)

investigated the 3 Li^+/V_2O_5 insertion/extraction properties by lowering the low voltage limit to 1.5 V (vs. Li/Li^+). Similar to the earlier study, cells were discharged/charged for 5 cycles each at 5 different current densities (100, 250, 500, 750, and 1000 mA g^{-1}) before returning to the initial current rate (100 mA g^{-1}) at cycle 26 to repeat the sequence. The galvanostatic charge-discharge rate performance is summarized in Fig. 5a. Similar to the 2 Li^+/V_2O_5 insertion/extraction performance, the first five cycles at 100 mA g^{-1} (C/4.3) were somewhat unstable with an insertion capacity of 429 mAh g^{-1} and a coulombic efficiency of 103% in cycle 5. The capacity is close to the theoretical capacity of 441 mAh g^{-1} for 3 Li^+/V_2O_5 insertion/extraction in crystalline V_2O_5. When the rate was increased to 250 mA g^{-1} (C/1.4), the cell was stabilized with an insertion capacity of 338 mAh g^{-1} and a coulombic efficiency of 100%. High insertion capacities of 280, 250, and 236 mAh g^{-1} were obtained at rates of 500 (1.8C), 750 (3.0C), and a 1000 (4.2C) mA g^{-1}, respectively, with coulombic efficiencies of ~100%. When the current was returned to 100 mA g^{-1} in cycle 26–30, an insertion capacity of 405 mAh g^{-1} was achieved. Comparing to cycle #5, the capacity retention was ~94%. Insertion capacities of 330, 273, 244, and 233 mAh g^{-1} were obtained at current rates of 250, 500, 750, and 1000 mA g^{-1}, respectively, in cycles 31–50, retaining ~98% of the corresponding capacities in cycle 6–25.

Charge-discharge curves at current rates of 100 (black), 250 (red), 500 (blue), 750 (magenta), and 1000 (green) mA g^{-1} are presented in Fig. 5b. All profiles retain the nearly linear feature as those in the 2 Li^+/V_2O_5 insertion/extraction processes. The shape of the charge-discharge curves is consistent with those of rGO/V_2O_5–$LiBO_2$ glass composite materials in the same potential range [18]. The stabilized CV curves in Fig. 5c show nearly ideal pseudocapacitive features with flat baselines and a large separation between the forward and backward scans. In addition, the first negative scan in Fig. S12 showed similar CV features as Fig. 4c, with a large reduction peak at ~2.3 V corresponding to the phase transformation from α-LiV_2O_5 to γ-$Li_2V_2O_5$ with the intermediate phase superimposed. A further downward dip was observed at 1.5 V corresponding to the phase transformation from γ- $Li_2V_2O_5$ to rock-salt-type ω-$Li_xV_2O_5$ ($2 < x < 3$). However, the oxidation peaks in the reversed positive scan overlapped into a broad wave spreading from 2.0 to 3.5 V. Both the large reduction peak at 2.3 V and the broad oxidation wave disappeared in the 2nd cycle (red), showing only the smooth capacitive features. This behavior is consistent with literature [14], showing that the transformation into the rock-salt structure by 3 Li^+/V_2O_5 insertion irreversibly damages the crystal structure and converts it into a fully amorphous structure. Notably, the CV curves after the 1st cycle became stabilized. Both Fig. 5b and c indicate that Li storage is dominated by the large pseudocapacitance. Fig. 5d demonstrates that a decent stability can be obtained with this mechanism in long cycling at 100 mA g^{-1}. The capacity slowly dropped from 442 mAh g^{-1} in cycle 3 to 310 mAh g^{-1} in cycle 100, retaining 70% of the original value. The results in Fig. 5c are a great leap from the extensive studies seeking using crystalline V_2O_5 materials for 3 Li^+/V_2O_5 processes [14]. It is attributed to the novel properties of the CNF–V_2O_5 core-shell hybrid structure. The scalable capability of electrospinning and electrodeposition may provide a viable method to push the core-

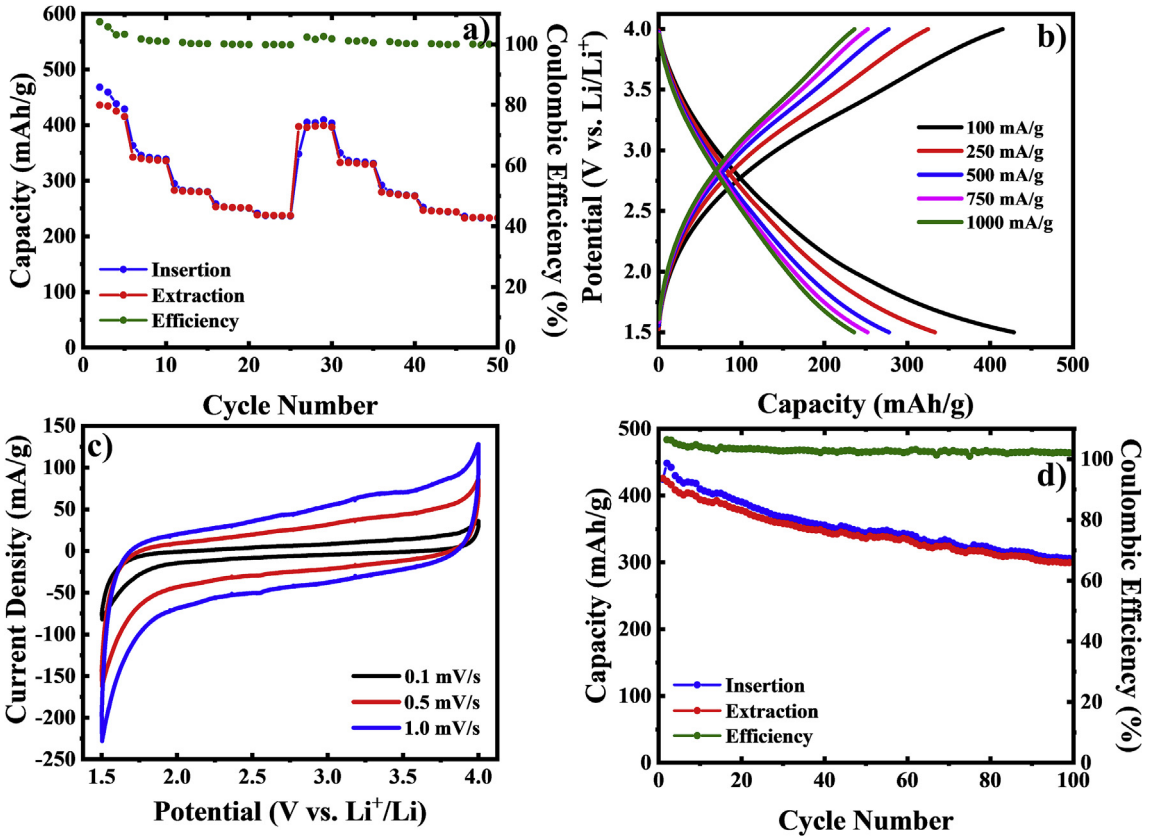

Fig. 5. Electrochemical characterization of the 3 Li^+/V_2O_5 insertion/extraction. a) Rate performance of the CNF–V_2O_5 core-shell structure in the potential range of 4.0–1.5 V (vs. Li/Li^+) at 5 different current density values (100, 250, 500, 750, and 1000 mA g^{-1}), each with 5 charge-discharge cycles. b) The galvanostatic charge-discharge profiles of the last cycle at each current density in the rate performance. c) Cyclic voltammetry curves at 0.1 (black), 0.5 (red) and 1.0 (blue) mV s^{-1} in the potential range of 4.0–1.5 V (vs. Li/Li^+). d) Long-term cycling at a rate of 100 mA g^{-1}. (For interpretation of the references to color in this figure legend, the reader is referred to the Web version of this article.)

shell concept involving amorphous V_2O_5 materials [39,40] closer to LIB applications.

3.5. Discussion on the novel properties of amorphous V_2O_5 cathodes

Table S1 and Table S2 compare the performance of the CNF–V_2O_5 core-shell structure in 2 Li^+/V_2O_5 and 3 Li^+/V_2O_5 insertion/extraction, respectively, with an extensive list of studies in literature. For 2 Li^+/V_2O_5 insertion/extraction, the CNF–V_2O_5 core-shell structure is among the top judging by both the specific capacity and current density (or C rates). For 3 Li^+/V_2O_5 insertion/extraction, the advantages of CNF–V_2O_5 core-shell structure in terms of specific capacity and current density (or C rates) are even more evident. In addition, the improved stability and the potential for scalable production of the CNF–V_2O_5 core-shell structure by electrospinning and pulsed electrodeposition make it attractive for future LIB developments.

So far extensive efforts are being made to attain the high capacity at high power rates by improving ion diffusion using nanostructured V_2O_5 materials, particularly 2D nanosheets [17]. Interestingly, the rate-performance curves of the 2 Li^+/V_2O_5 process (Fig. 4a) and 3 Li^+/V_2O_5 process (Fig. 5a) in this study show a common phenomenon, i.e. a high specific capacity was retained at a relatively high current density of 1000 mA g^{-1}, which is not obtainable with traditional micron-sized V_2O_5 materials. As demonstrated in a study by Rui et al. [53], the rate-performance curve of few-layer V_2O_5 nanosheets (2.1–3.8 nm thick) shift upward by ~100 mAh g^{-1} comparing to that of bulk V_2O_5 crystals (1–4 μm in size). Here we have obtained a stable high capacity of 198 mAh g^{-1} at a high rate of 1000 mA g^{-1} (~5C) for 2 Li^+/V_2O_5 process, comparable to the reports with few-layer V_2O_5 nanosheets [53] and V_2O_5 nanoparticles anchored on CNTs [54]. More importantly, we were able to obtain a relatively high stable capacity of 236 mAh g^{-1} at the high rate of 1000 mA g^{-1} (~4C) for the 3 Li^+/V_2O_5 process, which have not been obtained with nanostructured V_2O_5 alone. In our previous study using the hybrid structure of V_2O_5 shells on vertically aligned carbon nanofiber cores [40], we have observed that the rate-performance curve of the amorphous V_2O_5 shells shift up by ~60 mAh g^{-1} in 2 Li^+/V_2O_5 process and by ~150 mAh g^{-1} in 3 Li^+/V_2O_5 process comparing to the crystalline V_2O_5 shells. Those observations are consistent with the results in this study, which demonstrate that the core-shell hybrid structure is effective to facilitate the high-capacity and high-power capability of amorphous V_2O_5 materials. It is particularly attractive for future batteries involving larger ions such as Na^+ or polyvalent ions such as Mg^{2+}, which may benefit from the more open structure of amorphous V_2O_5 materials.

4. Conclusion

In summary, self-sustained CNF membranes fabricated by carbonizing electrospun PAN nanofibers were used as 3D porous LIB electrodes. A thin V_2O_5 layer was coated onto the CNFs using a pulsed electrodeposition from a V_2O_5 sol solution. SEM, HRTEM and XRD analysis confirmed that the CNF–V_2O_5 core-shell structure consisted of a uniform coaxial V_2O_5 layer (30–50 nm in thickness) on the continuous CNF core throughout the whole membrane. After 4 h of thermal annealing at 300 °C in the air, the V_2O_5 shell presents

a partially hydrated amorphous material. Electrochemical characterization in the potential range of 4.0–2.0 V (vs Li/Li^+) revealed that the V_2O_5 shell in this core-shell structure present reversible 2 Li^+/V_2O_5 insertion/extraction with a near theoretical capacity of 291 mAh g^{-1} and excellent stability even at high rates. There was nearly no capacity fading after 100 cycles. Moreover, when the potential range was extended to 4.0–1.5 V (vs Li/Li^+), a high capacity of 429 mAh g^{-1} was obtained corresponding to reversible 3 Li^+/V_2O_5 insertion/extraction. A relatively high capacity retention of 70% was obtained after 100 cycles. These results demonstrated that the CNF–V_2O_5 core-shell structure is an effective approach to breaking the intrinsic limits of crystalline V_2O_5 and enabling amorphous V_2O_5 materials to be used as a promising scalable high-capacity LIB cathode.

Acknowledgments

We would like to thank Jacob Hughes and Brice Lacroix at Kansas State University (KSU) for the Raman Spectroscopy analysis, Shah Valloppilly at the University of Nebraska Center for Materials and Nanoscience (NCMN) for XRD analysis, Steve Michalski at NCMN for BET measurements, Xingzhang Li and Anand Sarella at NCMN for TEM imaging, and Dan Boyle of KSU for helping with SEM imaging. We would also like to give special thanks to Manomi Perera, Chamara Gunawardana and Christer Aakeröy of KSU for their help in the TGA analysis and Dr. Changsang Yun of Seoul National University for assistance in electrospinning nanofibers. This work was supported by a NASA grant NNX13AD42A and NSF grants CBET-1703263 and DMR-1707585.

Appendix A. Supplementary data

Supplementary data related to this article can be found at https://doi.org/10.1016/j.electacta.2018.02.167.

References

[1] E. Karden, S. Ploumen, B. Frickea, T. Miller, K. Snyder, Energy storage devices for future hybrid electric vehicles, J. Power Sources 168 (2007) 2–11.
[2] M. Armand, J.M. Tarascon, Building better batteries, Nature 451 (2008) 652–657.
[3] F. Díaz-González, A. Sumper, O. Gomis-Bellmunt, R. Villafáfila-Robles, A review of energy storage technologies for wind power applications, renew, Sustainable Energy Rev. 16 (2012) 2154–2171.
[4] B. Scrosati, J. Garche, Lithium batteries: status, prospects and future, J. Power Sources 195 (2010) 2419–2430.
[5] X. Luo, J. Wang, M. Dooner, J.C. Clarke, Overview of current development in electrical energy storage technologies and the application potential in power system operation, Appl. Energy 137 (2015) 511–536.
[6] H.D. Yoo, E. Markevich, G. Salitra, D. Sharon, D. Aurbach, On the challenge of developing advanced technologies for electrochemical energy storage and conversion, Mater. Today 17 (2014) 110–121.
[7] J.R. Szczech, S. Jin, Nanostructured silicon for high capacity lithium battery anodes, Energy Environ. Sci. 4 (2011) 56–72.
[8] C.K. Chan, H.L. Peng, G. Liu, K. Mcllwrath, X.F. Zhang, R.A. Huggins, Y. Cui, High-performance lithium battery anodes using silicon nanowires, Nat. Nanotechnol. 3 (2008) 31–35.
[9] S.A. Klankowski, R.A. Rojeski, B.A. Cruden, J. Liu, J. Wu, J. Li, A high-performance lithium-ion battery anode based on the core-shell heterostructure of silicon-coated vertically aligned carbon nanofibers, J. Mater. Chem. 1 (2013) 1055–1064.
[10] J. Xu, S. Dou, H. Liu, L. Dai, Cathode materials for next generation lithium ion batteries, Nano Energy 2 (2013) 439–442.
[11] J.W. Fergus, Recent developments in cathode materials for lithium ion batteries, J. Power Sources 195 (2010) 939–954.
[12] M.S. Whittingham, Ultimate limits to intercalation reactions for lithium batteries, Chem. Rev. 114 (2014) 11414–11440.
[13] M.S. Whittingham, Y. Song, S. Lutta, P.Y. Zavalij, N.A. Chernova, Some transition metal (oxy)Phosphates and vanadium oxides for lithium batteries, J. Mater. Chem. 15 (2005) 3362–3379.
[14] Y. Yue, H. Liang, Micro- and nano-structured vanadium pentoxide (V2O5) for electrodes of lithium-ion batteries, adv, Energy Mater (2017) 1602545.
[15] J. Cheng, B. Wang, H.L. Xin, G. Yang, H. Cai, F. Niea, H. Huang, Self-assembled V_2O_5 nanosheets/reduced graphene oxide hierarchical nanocomposite as a high-performance cathode material for lithium ion batteries, J. Mater. Chem. 1 (2013) 10814–10820.
[16] A. Moretti, S. Passerini, Bilayered nanostructured $V_2O_5 \cdot nH_2O$ for metal batteries, Adv. Energy Mater (2016) 1600868.
[17] X. Huang, X. Rui, H.H. Hng, Q. Yan, Vanadium pentoxide-based cathode materials for lithium-ion batteries: morphology control, carbon hybridization, and cation doping, Part. Part. Syst. Char. 32 (2015) 276–294.
[18] S. Afyon, F. Krumeich, C. Mensing, A. Borgschulte, R. Nesper, New high capacity cathode materials for rechargeable Li-ion batteries: vanadate-borate glasses, Sci. Rep. 4 (2014) 7113.
[19] F. Mattelaer, K. Geryl, G. Rampelberg, J. Dendooven, C. Detavernier, Amorphous, Crystalline Vanadium, Oxides as high-energy and high-power cathodes for three-dimensional thin-film lithium ion batteries, ACS Appl. Mater. Interfaces 9 (2017) 13121–13131.
[20] Q. Liu, Z.-F. Li, Y. Liu, H. Zhang, Y. Ren, C.-J. Sun, W. Lu, Y. Zhou, L. Stanciu, E.A. Stach, J. Xie, Graphene-modified nanostructured vanadium pentoxide hybrids with extraordinary electrochemical performance for Li-Ion batteries, Nat. Commun. 6 (2015) 1–10.
[21] Y. Liu, E. Uchaker, N. Zhou, J. Li, Q. Zhanga, G. Cao, Facile synthesis of nanostructured vanadium oxide as cathode materials for efficient Li-ion batteries, J. Mater. Chem. 22 (2012) 24439–24445.
[22] C. Wang, Y. Cao, Z. Luo, G. Li, W. Xu, C. Xiong, G. He, Y. Wang, S. Li, H. Liu, D. Fang, Flexible potassium vanadate nanowires on Ti fabric as a binder-free cathode for high-performance advanced lithium-ion battery, Chem. Eng. J. 307 (2017) 382–388.
[23] D. Fang, L. Li, W. Xu, G. Li, Z. Luo, C. Liang, Y. Ji, J. Xu, C. Xiong, Self-assembled hairy ball-like V_2O_5 nanostructures for lithium ion batteries, RSC Adv. 4 (2014) 25205.
[24] Y. Cao, D. Fang, C. Wang, L. Li, W. Xu, Z. Luo, X. Liu, C. Xiong, S. Liu, Novel aligned sodium vanadate nanowire arrays for high-performance lithium-ion battery electrodes, RSC Adv. 5 (2015) 42955.
[25] Y. Cao, D. Fang, R. Liu, M. Jiang, H. Zhang, G. Li, Z. Luo, X. Liu, J. Xu, W. Xu, C. Xiong, Three-dimensional porous iron vanadate nanowire arrays as a high performance lithium-ion battery, ACS Appl. Mater. Interface 7 (2015) 27685–27693.
[26] C. Zhang, Z. Chen, Z. Guo, X.W. Lou, Additive-free synthesis of 3D porous V2O5 hierarchical microspheres with enhanced lithium storage properties, Energy Environ. Sci. 6 (2013) 974–978.
[27] G.-M. Wu, A.-R. Wang, M.-X. Zhang, H.-Y. Yang, B. Zhou, J. Shen, Investigation on properties of V_2O_5–MWCNTs composites as cathode materials, J. Sol. Gel Sci. Technol. 46 (2008) 79–85.
[28] B. Sun, K. Huang, X. Qi, X. Wei, J. Zhong, Rational construction of a functionalized V_2O_5 nanosphere/MWCNT layer-by-layer nanoarchitecture as cathode for enhanced performance of lithium-ion batteries, Adv. Funct. Mater. 25 (2015) 5633–5639.
[29] J.H. Lee, J.-M. Kim, J.-H. Kim, Y.-R. Jang, J.A. Kim, S.-H. Yeon, S.-Y. Lee, Toward ultrahigh-capacity V_2O_5 lithium-ion battery cathodes via one-pot synthetic route from precursors to electrode sheets, Adv. Mater. Interfaces 3 (2016) 1600173.
[30] R. Yu, C. Zhang, Q. Meng, Z. Chen, H. Liu, Z. Guo, Facile synthesis of hierarchical networks composed of highly interconnected V_2O_5 nanosheets assembled on carbon nanotubes and their superior lithium storage properties, ACS Appl. Mater. Interfaces 5 (2013) 12394–12399.
[31] K.H. Seng, J. Liu, Z.P. Guo, Z.X. Chen, D. Jia, H.K. Liu, Free-standing V_2O_5 electrode for flexible lithium ion batteries, Electrochem. Commun. 13 (2011) 383–386.
[32] Y. Yang, L. Li, H. Fei, Z. Peng, G. Ruan, J.M. Tour, Graphene Nanoribbon/V_2O_5 cathodes in lithium-ion batteries, ACS Appl. Mater. Interfaces 9 (2014) 9590–9594.
[33] G.P. Pandey, T. Liu, E. Brown, Y. Yang, Y. Li, X.S. Sun, Y. Fang, J. Li, Mesoporous hybrids of reduced graphene oxide and VanadiumPentoxide for enhanced performance in lithium-ion batteries and electrochemical capacitors, ACS Appl. Mater. Interfaces 8 (2016) 9200–9210.
[34] D. Chen, H. Quan, S. Luo, X. Luo, F. Deng, H. Jiang, Reduced graphene oxide enwrapped vanadium pentoxide nanorods as cathode materials for lithium-ion batteries, Physica E 56 (2014) 231–237.
[35] S.H. Choi, Y.C. Kang, Uniform decoration of vanadium oxide nanocrystals on reduced graphene-oxide balls by an aerosol process for lithium-ion battery cathode material, Chem. Eur. J. 20 (2014) 6294–6299.
[36] H. Zhao, L. Pan, S. Xing, J. Luo, J. Xu, Vanadium oxides-reduced graphene oxide composite for lLithium-ion batteries and supercapacitors with improved electrochemical performance, J. Power Sources 22 (2013) 21–31.
[37] D. Pham-Cong, K. Ahn, S.W. Hong, S.Y. Jeong, J.H. Choi, C.H. Doh, J.S. Jin, E.D. Jeong, C.R. Cho, Cathodic performance of V_2O_5 nanowires and reduced graphene oxide composites for lithium ion batteries, Curr. Appli. Phys. 14 (2014) 215–221.
[38] Y. Cao, D. Chai, Z. Luo, M. Jiang, W. Xu, C. Xiong, S. Li, H. Liu, D. Fang, Lithium vanadate Nanowires@Reduced graphene oxide nanocomposites on titanium foil with super high capacities for lithium-ion batteries, J. Colloid Interface Sci. 498 (2017) 210–216.
[39] X. Chen, H. Zhu, Y.-C. Chen, Y. Shang, A. Cao, L. Hu, G.W. Rubloff, MWCNT/V_2O_5 core/shell sponge for high areal capacity and power density Li-Ion cathodes, ACS Nano 6 (2012) 7948–7955.
[40] E. Brown, J. Acharya, G.P. Pandey, J. Wu, J. Li, Highly stable three lithium

insertion in thin V_2O_5 shells on vertically aligned carbon nanofiber arrays for ultrahigh-capacity lithium ion battery cathodes, Adv. Mater. Interfaces (2016) 1600824.
[41] S.-H. Park, W.-J. Lee, Hierarchically mesoporous carbon Nanofiber/Mn_3O_4 coaxial nanocables as anodes in lithium ion batteries, J. Power Sources 281 (2015) 301–309.
[42] S.-H. Park, W.-J. Lee, Hierarchically mesoporous CuO/carbon nanofiber coaxial shell-core nanowires for lithium ion batteries, Sci. Rep. 5 (2015) 9754.
[43] E. Uchaker, Y.Z. Zheng, S. Li, S.L. Candelaria, S. Hu, G.Z. Cao, Better than crystalline: amorphous vanadium oxide for sodium-ion batteries, J. Mater. Chem. 2 (2014) 18208–18214.
[44] J. Liu, J. Essner, J. Li, Hybrid supercapacitor based on coaxially coated manganese oxide on vertically aligned carbon nanofiber arrays, Chem. Mater. 22 (2010) 5022–5030.
[45] Y. Fang, J. Liu, D.J. Yu, J.P. Wicksted, K. Kalkan, O. Topal, B.N. Flanders, J. Wu, J. Li, Self-supported supercapacitor membranes: polypyrrole-coated multi-walled carbon nanotube networks enabled by pulsed electrodeposition, J. Power Sources 195 (2010) 674–679.
[46] T. Singh, S. Wang, N. Aslam, H.Z. Zhang, S. Hoffmann-Eifert, S. Mathur, Atomic layer deposition of transparent VO_x thin films for resistive switching applications, Chem. Vap. Depos. 20 (2014) 291–297.
[47] R. Baddour-Hadjean, M.B. Smirnov, K.S. Smirnov, V.Y. Kazimirov, J.M. Gallardo-Amores, U. Amador, M.E. Arroyo-de Dompablo, J.P. Pereira-Ramos, Lattice dynamics of β-V_2O_5: Raman spectroscopic insight into the atomistic structure of a high-pressure vanadium pentoxide polymorph, Inorg. Chem. 51 (2012) 3194–3201.
[48] Q. Su, X.Q. Liu, H.L. Ma, Y.P. Guo, Y.Y. Wang, Raman spectroscopic characterization of the microstructure of V_2O_5 films, J. Solid State Electrochem. 12 (2008) 919–923.
[49] A. Moretti, F. Maroni, I. Osada, F. Nobili, S. Passerini, V_2O_5 aerogel as a versatile cathode material for lithium and sodium batteries, Chem Electrochem 2 (2015) 529–537.
[50] J. Lee, A. Urban, X. Li, D. Su, G. Hautier, G. Ceder, Unlocking the potential of cation-disordered oxides for rechargeable lithium batteries, Science 343 (2014) 519–522.
[51] S. Passerini, D.B. Le, W.H. Smyrl, M. Berrettoni, R. Tossici, R. Marassi, M. Giorgetti, XAS and electrochemical characterization f lithiated high surface area V_2O_5 aerogels, Solid State Ion. 104 (1997) 195–204.
[52] K. Takahashi, Y. Wang, G. Cao, Ni–$V_2O_5 \cdot nH_2O$ Core–Shell nanocable arrays for enhanced electrochemical intercalation, J. Phys. Chem. B 109 (2005) 48–51.
[53] X. Rui, Z. Lu, H. Yu, D. Yang, H.H. Hng, T.M. Lim, Q. Yan, Ultrathin V_2O_5 nanosheet cathodes: realizing ultrafast reversible lithium storage, Nanoscale 5 (2013) 556–560.
[54] Y.-S. Hu, X. Liu, J.-O. Müller, R. Schlögl, J. Maier, D.S. Su, Synthesis, Electrode Performance, Of nanostructured V_2O5 by using a carbon tube-in-tube as a nanoreactor and an efficient mixed-conducting network, Angew. Chem. Int. Ed. 48 (2009) 210–214.